Analysis of a boundary layer of a granular mixture flowing past a plate at zero incidence

Sandro Longo [a,*], Alessandro Valiani [b]

[a] Department of Civil Engineering, University of Parma, Parco Area delle Scienze, 181/A, 43124 Parma, Italy
[b] Department of Civil Engineering, University of Ferrara, Via Saragat, 1, 44122 Ferrara, Italy

ABSTRACT

The present paper reports experiments on the flow field of a grain–water mixture around a flat, thin plate at zero incidence. The velocity measurements are performed using a Particle Image Velocimetry (PIV) technique. The Proper Orthogonal Decomposition (POD) analysis reveals that the degree of organisation of the flow field increases with the Reynolds number. The displacement thickness of the boundary layers generally increases downstream and increases slightly with the Reynolds number, which is based on the length of the plate. The vorticity normal to the plane of the flow has a maximum value at the leading edge and is almost invariant with respect to the Reynolds number; additionally, the non-dimensional profiles in the direction normal to the plate show self-similarity in the streamwise direction for a single test, and the profiles are almost coincident for all tests. The flow divergence is assumed to be an indicator of the variation of the sediment volume concentration; it indicates an increment of the sediment volume concentration near the walls of the plate and a spatial periodicity downstream that is triggered for relatively large Reynolds numbers. The spatial correlation analysis allows the evaluation of the integral length scales that are successively utilised in modelling the non-local rheology of the mixture. The velocity profiles have been modelled based on Savage's model and Bagnold's experiments, with further modifications from Ertaş and Halsey (2002) that are represented by pseudo-turbulence modelling of the flow field. Vortices have been detected according to the λ_2-criterion given by Jeong and Hussain (1995). The statistics of the vortices indicate that no preferential size is selected and that at a high Reynolds number, the most energetic vortices develop near the leading edge.

© 2014 Elsevier Masson SAS. All rights reserved.

1. Introduction

Boundary layers are widely studied in Newtonian fluid flows and represent a benchmark for several models of turbulence and for the analysis of coherent structures. The concept of the boundary layer has been successful in Newtonian fluid dynamics because it is quite effective in reducing the complexity of the flow, separating an external region by an internal region that is in contact with the rigid surface and where the no-slip condition is satisfied. Boundary layers also occur in non-Newtonian fluids, e.g., in dry granular flows and in mixtures of liquid and grains. In the literature, there are extended analyses of free surface boundary layers in dry granular flows in rotating drums [1–3] and of dry granular flows in contact with flat walls (e.g., [4]). In these studies, the motion is

due to gravity, but to our knowledge, the analysis of the boundary layer of a mixture of grains at a high volumetric concentration and water is limited. More data and analyses are available for boundary layers at the interface between the liquid and grains at the bottom, with a strong vertical variation in the volumetric concentration of the grains, as occurs in natural rivers, but the limited thickness of the granular layers complicates the quantitative analysis of the structure of the flow within the layer.

For boundary layers of dry granular streams that are in contact with walls, the additional problem of the correct boundary conditions arises because, according to several constraints, either slip or no-slip conditions may occur. In the slip condition, the slip velocity can be calculated using several models, with a huge variety of possible results [5].

For boundary layers of a mixture of water and grains, the analysis is even more complicated because (1) the rheology is not completely known and properly described and (2) the boundary conditions are not simple. Since the work of [6], very few improvements have been made in characterising the effects of the

* Corresponding author. Tel.: +39 0521 90 5157; fax: +39 0521 90 5924.
E-mail address: sandro.longo@unipr.it (S. Longo).

List of symbols

$\widetilde{\cdots}$	Non-dimensional operator
$\overline{\cdots}$	Ensemble average operator, mean value
α	Exponent
β_0, β_1	Constants
δ	Thickness of the gap, displacement thickness of the boundary layer
ϕ_D	Dynamic internal friction angle
Γ	Shear rate, circulation
λ	Linear concentration of the solid phase, wavelength
μ	Dynamic inter-particle fluid viscosity
ν	Kinematic viscosity of the inter-particle fluid
$\nu_{mixture}$	Equivalent kinematic viscosity of the mixture
ρ_s, ρ_s'	Mass density of the solid phase, submerged value
$\sigma, \sigma^0, \sigma^*$	Normal stress, equilibrium normal stress, dissipative normal stress
τ, τ^0, τ^*	Shear stress, equilibrium shear stress, dissipative shear stress
θ	Momentum thickness of the boundary layer
$\omega, \omega_c, \omega_z$	Rotation rate, critical rotation rate, vorticity component along z
χ	Double velocity correlation, coefficient
μ_0, μ_1	Consistency indexes in Bagnold's model
a_1, a_2, a_3, a_4	Coefficients
b	Function
Ba	Bagnold number
C, C_r, C_0, C_*, C_m	Volumetric concentration of the grains (ratio between the volume of sediments and the bulk volume), maximum volumetric concentration of the grains at rest, volumetric concentration at which fluidity occurs, densest possible volumetric concentration, maximum volumetric concentration at which continued shearing can occur
CCW	Counter-clockwise
CW	Clockwise
d	Grain diameter
D	Rate of deformation tensor
g	Acceleration of gravity
k	Constant
l	Length of the plate
L	Integral length scale
PIV	Particle Image Velocimetry
PMMA	Polymethyl methacrylate
POD	Proper Orthogonal Decomposition
R	Radius of the cylinder (internal, external), non-dimensional double velocity correlation
r	Radius of the eddies
rpm	Revolutions per minute
Re_l, Re_x	Reynolds number based on the length of the plate, on the distance from the leading edge
T, **T**^{0}, **T***	Stress tensor, equilibrium stress tensor, dissipative stress tensor
t	Time
Ta, Ta$_c$	Taylor's number, critical Taylor's number
U_0	Reference asymptotic velocity
U, V	Horizontal, vertical instantaneous velocity
U', V'	Horizontal, vertical fluctuating velocity
x, y	Spatial coordinates
x	Position vector

and ad hoc assumptions are often necessary for the closure. While the liquid satisfies the no-slip condition at the solid boundaries, the grains exhibit a variety of behaviours, including gas-like behaviour that is dominated by collisions, fluid-like behaviour with long-term contacts, and solid-like behaviour that is dominated by the static or quasi-static transfer of stress. For the grains, the slip condition is present in the gas-like regime, whereas in the solid-like regimes, the slip condition is almost completely inhibited. The inherent nonlinear behaviour due to friction can also favour the generation of shear bands that continuously and apparently randomly appear and disappear in the flow field. These local behaviours strongly influence the external flow field and require proper models.

Numerous models of sediment transport in a two-phase flow, with water and grains at a high volume concentration, are based on the detailed analysis of the dynamics of the two phases, including the interaction between the two phases. The simplest model is based upon transport in a sheet-flow condition that is uniform in the horizontal direction (e.g., [7]), but the use of more complex models extended to three dimensions increases the accuracy. The first and most challenging task is to correctly describe the intergranular stresses, the influence of the grains on the fluid turbulence, and the interaction between the grains and the fluid. The second step is the solution of the nonlinear system of equations that describe the problem with several variables and numerous closure assumptions. There are several different descriptions of the stresses in the granular and fluid phases, and in the early attempts to solve the equations, certain variables such as the turbulent viscosity or the sediment volume concentration were fixed. At high volume concentrations of the grains, the inter-particle fluid flow plays a progressively reduced role and the grain dynamics become more dominant, with behaviour similar to dry grains mixtures.

Numerous analogies between granular mixtures and turbulent flows have been proposed, as clusters of particles in granular streams have been observed in experiments [8] and have been included in models under the description of 'granular eddies' [9], i.e., a large-scale, condensed structure of particles moving coherently. Hence, eddies in granular mixtures are relevant for models in which the non-locality of the rheology is included [10]. In addition to the natural length scales governing the motion, represented by the diameter of the grains and by the geometric scales of the obstacles or other length macro scales, new length scales represented by the size of the granular eddies may become relevant.

The present paper analyses the flow field of a grain–water mixture around a flat, thin plate at zero incidence, with a specific effort to detect the length scales associated with coherent structures. A mixture of local and non-local rheology is adopted to model the velocity profiles, in which the local rheology is based on Savage's model and the non-local rheology is based on the concept of the viscous length scale [9]. Additional information has been gained from the distribution and partition of the vortices. The paper is organised as follow. The experimental set-up and the description of the experiments are detailed in Section 2. Section 3 contains the analysis of the results, with the description of the flow field and of the boundary layer geometry. It also contains the analysis of the vorticity and of the spatial correlations. Section 4 is devoted to the modelling of the velocity profiles in the boundary layer and Section 5 reports the analysis of the vortices. The last Section contains the conclusions.

2. Methodology

2.1. Experimental set-up

To generate stationary flux of the granular mixture, a concentric-cylinder, Taylor–Couette shear cell was used (Fig. 1), and the surface of the internal cylinder was roughened with sand paper to

interstitial fluid, and numerous models are still based on rheology that was developed for dry granular streams. Unfortunately, Bagnold's model does not include the effects of solid boundaries
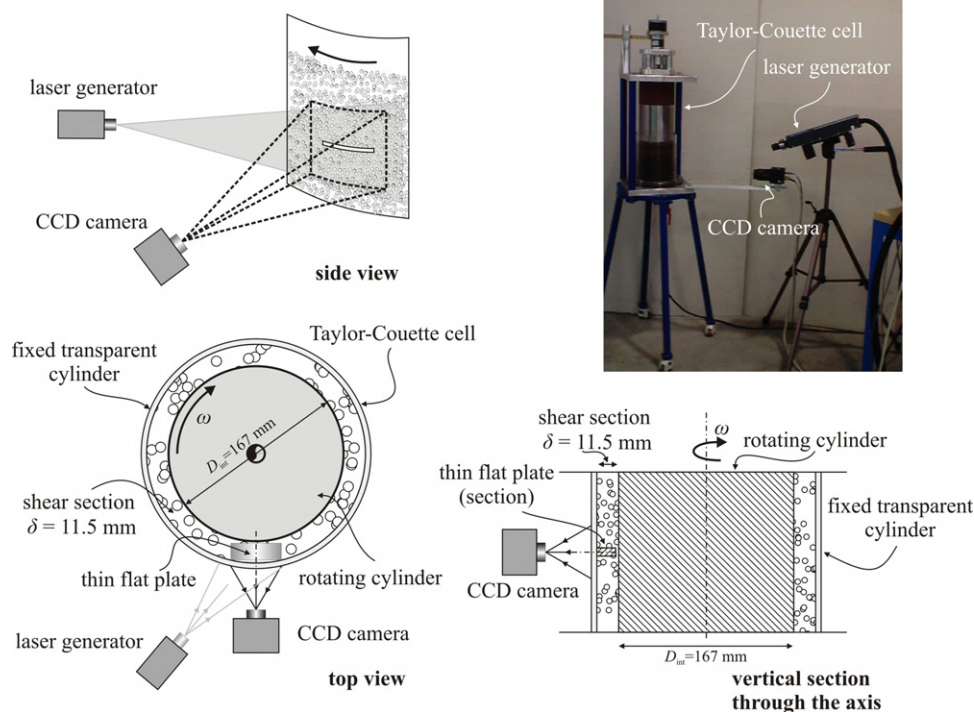
Fig. 1. Experimental setup.

yield more efficient momentum transfer. The internal rotating vertical cylinder is made of stainless steel with a diameter $D_{int} = 167$ mm and the external fixed cylinder is made of Polymethyl methacrylate (PMMA) with a diameter $D_{ext} = 190$ mm. The radius ratio is equal to $D_{ext}/D_{int} = 1.137$. The height of the cell is 340 mm, the wall thickness of the external fixed cylinder is $s = 5$ mm and the annular gap between cylinders, representing the shear section, is $\delta = 11.5$ mm.

The device and the general setup are described in detail in [11,12]. Tests were carried out with a mixture of water and artificial clay grains that were sorted to have a diameter of $d = 0.25$–0.50 mm. The grains were almost spherical and had a relative (respect to the water) specific weight nearly equal to 1.0 due to gas that was trapped during the production process. A specific weight almost equal to the specific weight of water reduces the gravitational effects to a minimum and avoids a significant normal interparticle stress increment in the vertical direction. The maximum solid fraction, defined as the ratio between the volume of sediment and the bulk volume, for random packing was determined by measuring the bulk volume of the grains at rest, the weight of the sample and the specific weight; the obtained value was $C_r = 0.643$. During motion, the solid fraction is reduced, reaching an average granular volumetric concentration of $C \approx 0.56$. The temperature during the tests was equal to 19.5 °C, with fluctuations no larger than 1 °C.

The measurements were carried out using a commercial TSI Particle Image Velocimetry (PIV) with a 2048 × 2048 pixel² video camera TSI Power View Model 630149, fitted with a Nikon NIKKOR AF D 50 mm/f lens with an adapter ring Nikon PK-12, which increases the focal length by 14 mm. The light source was a Solo Nd: YAG III dual laser head with a maximum repetition rate of 15 Hz and an output energy of 50 mJ. The laser was water-cooled and mounted on the same side of the cylinder as the video camera. The layout is shown in Fig. 1. The lenses of the laser systems were arranged to generate a light spot that was able to illuminate the area detected in the frames of the video camera. Polarised lenses were added to the video camera to eliminate reflections. The video camera records the light scattered by the grain particles moving

near the internal wall of the polymethyl methacrylate (PMMA) cylinder.

Pairs of images were acquired with a frequency of 3.75 Hz, and the time interval between the two images ranged from 1000 to 3000 μs depending on the maximum particle velocity and the gradient of the velocity. A quadratic polynomial transformation was applied to correct the acquired data (see [11]).

The velocity computation was performed with TSI software based on the correlation analysis of two different frames, using an interrogation window of 32 × 32 pixel² ($\approx 8 \times 8d^2$) with a 50% overlap. The result is a matrix of vectors at the grid nodes that are 16 pixels, or 1.54 mm ($\approx 4d$), apart. For each test, 100 pairs of frames were acquired, which corresponded to approximately 27 s of data. After the correlation analysis was complete, the outliers were rejected by the cellular neural network method [13]. The percentage of vectors that were rejected varied from 5% to 12%.

2.2. Experiments

The boundary layer developed on both faces of a thin aluminium plate, with a thickness of 1 mm and a length of 95 mm, that was attached to the external fixed cylinder 50 mm above the bottom of the Taylor–Couette cell. The free surface of the water when at rest was 150 mm above the bottom, while the grain bottom (the interface between water and grains at rest) was 20 mm below the free surface. A gap of to 1.5 ± 0.3 mm was present between the obstacle and the internal rotating cylinder to avoid particle locking. At the maximum rotation rate of the internal cylinder, the mixture was almost homogeneous, and the mean volumetric concentration of the mixture was equal to $C = 0.559$, i.e., this value was reduced to 87% of the value at rest.

The measurements were acquired with a rotation rate ranging from 5 to 200 rpm, corresponding to a lateral velocity of the internal cylinder that ranged from 440 to 1760 mm/s. Initial tests without any obstacle showed an essentially regular flow field with limited shearing in the radial direction and in the horizontal plane. The actual mean value of the shear rate in the radial direction was

Table 1
Set of experiments with a flat plate at zero incidence angle.

Imposed rotation rate (rpm)	Computed lateral velocity of the driving wall (mm/s)	Measured asymptotic velocity of flow U_0 (at the transparent wall) (mm/s)	Computed mean radial shear rate $\approx$(s^{-1})	Re_l (.)
5	44	38	0.6	17
10	88	76	1.1	34
20	176	136	3.8	61
50	440	273	15.9	122
150	1320	607	67.9	272
200	1760	653	105	300

less than the theoretical value due to the existence of a boundary layer near the driving wall where the pseudo-temperature (a measure of the velocity fluctuations of the grains) level was high, with a consequent reduction in grain concentration. The bouncing of the sediments at the wall of the fixed transparent cylinder facilitates slip; hence, an almost uniform flow was obtained in the radial direction, with minimal effects from the curvature of the trajectories due to the annular gap.

The flow regime is described according to Bagnold's model in terms of the Bagnold number, defined as

$$\mathrm{Ba} = \frac{\rho_s d^2 \lambda^{1/2} \Gamma}{\mu}, \tag{1}$$

in which ρ_s is the density of the solid phase, d is the particle diameter, Γ is the shear rate, μ is the inter-particle fluid viscosity, and λ is the linear concentration of the solid phase, which is related to the solid volumetric concentration by

$$\lambda = 1/[(C_*/C)^{1/3} - 1], \tag{2}$$

in which C_* is the densest volumetric concentration of the grains. A Taylor–Couette flow can be unstable for a Taylor number larger than $\mathrm{Ta}_c \approx 1700$ [14]. The Taylor number, defined as

$$\mathrm{Ta} = \frac{\omega^2 R_{\mathrm{int}} (R_{\mathrm{ext}} - R_{\mathrm{int}})^3}{\nu_{mixture}^2}, \tag{3}$$

is the ratio between centrifugal and viscous forces and is used to quantify the limits of stability. In the conditions of the present experiments, the flow is always stable because, by assuming the equivalent viscosity of the mixture [6],

$$\nu_{mixture} = 2.2 \lambda^{3/2} \nu, \tag{4}$$

it can be shown that $\omega_c = 24.28$ rad/s ≈ 232 rpm, which is larger than the maximum rotation rate of the experiments.

The Reynolds numbers based on the distance from the leading edge and on the length of the plate are defined as

$$Re_x = \frac{U_0 x}{\nu_{mixture}}, \qquad Re_l = \frac{U_0 l}{\nu_{mixture}}. \tag{5}$$

The experimental conditions for the tests are listed in Table 1. Other experiments on the same device with circular cylinder and triangular cylinder obstacles have already been analysed from many aspects in [11,12].

3. Results and discussion

3.1. Flow velocity and boundary layer thickness

An overview of the degree of organisation of the motion can be obtained by examining the proper orthogonal decomposition (POD) of both the velocity and vorticity fields. The number of modes usually considered necessary for a global description of the flow field contains at least 90% of the total energy, with no residual mode carrying more than 1% of the total energy [15]. The results for
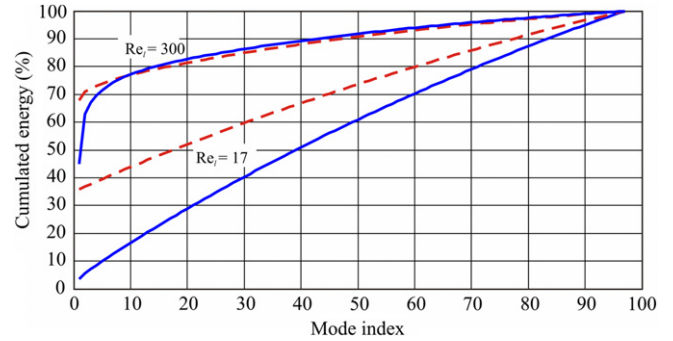
Fig. 2. Cumulative energy for POD of velocity (continuous curves) and of the vorticity (dashed curves).

two tests are shown in Fig. 2, which can be considered a spectral representation of the velocity and vorticity fields. The statistical convergence is obtained after $\approx$40 snapshots with an eigenvalue fluctuation of less than 1%. At the minimum Reynolds number, the minimum number of modes for velocity is equal to 83, whereas it is equal to 42 at the maximum Reynolds number. A decomposition of the vorticity modes is slightly more efficient than the velocity modes for lower Reynolds numbers, but the lower vorticity modes are always more energetic than the corresponding velocity modes. For example, the first mode of the vorticity POD accounts for almost 70% of the total energy at $Re_l = 300$, whereas the first mode of the velocity POD accounts for less than 45% of the total energy. Because the spectra decay at higher Reynolds numbers and are almost flat at lower Reynolds numbers, a progressive organisation of the motion is observed with increasing Reynolds numbers, with the emergence of the dominant modes accounting for most of the energy of the flow field. The level of organisation rapidly increases for $Re_l > 61$.

The average velocity field and the velocity computed according to the Blasius solution for a fluid with equivalent viscosity (Eq. (4)) are compared in Fig. 3. The difference between the viscous fluid flow and the present flow, when considering the general shape of the contour lines, is substantial for low Reynolds numbers but is not as significant for high Reynolds numbers.

Two different edges of the boundary layer have been computed: the displacement thickness, defined as

$$\delta = \int_0^\infty \left[1 - \frac{U(x, y)}{U_0(x)} \right] dy, \tag{6}$$

and the momentum thickness, defined as

$$\theta = \int_0^\infty \frac{U(x, y)}{U_0(x)} \left[1 - \frac{U(x, y)}{U_0(x)} \right] dy. \tag{7}$$

The measurements of the observed boundary layer structure are shown in Fig. 4, and the difference from the Newtonian fluid boundary layer at an equivalent Reynolds number is evident. The presence of the flat plate has effects that are upstream from the leading edge, with a range of influence that decreases with
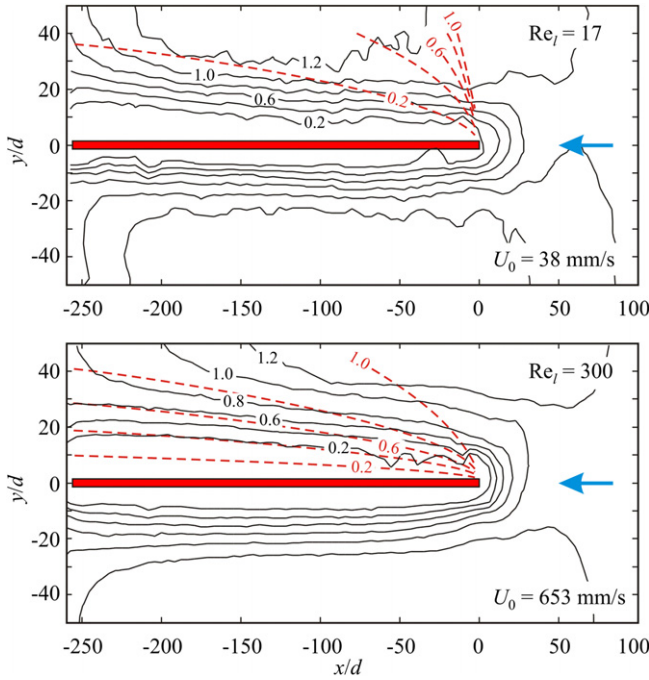
Fig. 3. The velocity fields described through contour lines at constant values of $|\boldsymbol{U}|/U_0$. The dashed lines refer to the Blasius solution for equivalent viscous Newtonian fluid. x and y indicate, respectively the horizontal and the vertical coordinate. The thick arrow represents the incoming asymptotic mean velocity of the mixture.

the Reynolds number. The distance where the effects are still observable is larger than 20 mm ($\approx 53d$) at $Re_l = 17$ and is equal to 10 mm ($\approx 27d$) at $Re_l = 300$. This upstream effect of the obstacle was also observed in tests with cylindrical bodies [11,12], in which a region of sediment at rest re-shaped the apparent upstream profile of the obstacles. Hence, the virtual origin of the boundary layer is not located at the leading edge but is upstream from the leading edge.

For granular boundary layers, the displacement thickness is slightly affected by the Reynolds number that is based on the distance from the origin (Re_x) and generally increases both downstream and with the Reynolds number that is based on length (Re_l). The latter behaviour is contrary to the characteristics of a laminar boundary layer of a viscous fluid. The momentum thickness is almost invariant downstream and increases with the Reynolds number (Re_l). For comparison, in Fig. 4 the equivalent boundary layer of a viscous fluid, characterised by displacement and a momentum thickness proportional to

$$\delta, \theta \propto \sqrt{\frac{\nu x}{U_0}}, \qquad (8)$$

is also shown. Not only is the growth rate different between the boundary layers of the present experiments, but the magnitude of the thickness of the mixture boundary layer is much larger than that of the homogeneous viscous fluid boundary layer; this effect is a consequence of frictional forces that are active in a large part of the domain near the wall. For free surface granular flows in a rotating drum, this frictional stress is dominant in most of the flowing layers [2].

The experimental velocity profiles for all the tests may collapse if they are non-dimensionalised with respect to the boundary layer thickness; in this case, the asymptotic value of the external stream is reached at more than twice the boundary layer thickness based on displacement; see Fig. 5, small panels. The details near the wall are missing due to the limited resolution of the PIV measurements;
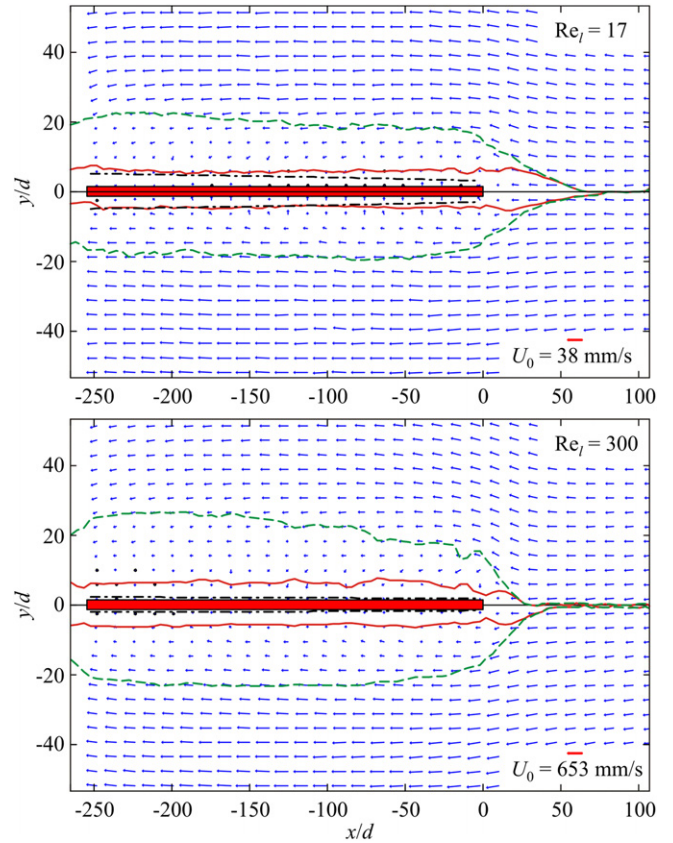

Fig. 4. Average velocity (100 couples of frames, ≈ 27 s) for tests at minimum and maximum Reynolds number (based on the length of the flat plate). The scale is different for the two tests and vectors shown are reduced to one third in the horizontal direction for a better visualisation. The dashed lines represent the displacement thickness, the thin lines represent momentum thickness, the dash–dot lines represent the equivalent viscous boundary layer displacement thickness.

nevertheless, a slip velocity is evident for tests at $Re_l = 122, 272$, and 300. The value of the slip velocity is strongly variable with the section of analysis and is related to the periodicity observed for the divergence (assumed to be related to the volumetric concentration), with larger values for reduced volumetric concentrations (see next Session 3.3). The slip condition disappears towards the trailing edge and is caused, in part, by the effect of the smoothness of the plate and by the effect of the disturbances of the leading edge due to the finite thickness of the plate. The interpolated velocity profiles are collected in the large panel in Fig. 5, and except for the data corresponding to the test at $Re_l = 34$, all curves show a fairly similar shape in most of the domain, with differences near the bottom due to slip velocity occurrence at higher Reynolds numbers. In some sections and near the wall, an inversion of the velocity is shown that is associated with stable coherent structures and resembles the recirculation cells observed in [11,12]) for triangular and circular cylinders. Hence, the flow field is characterised by its evident similarity with respect to the Reynolds number and the distance from the leading edge.

3.2. Vorticity

The dominant component of the vorticity is normal to the plane of the flow. The other components cannot be measured, but are generally negligible since the flow is almost plane. The non-dimensional vorticity for the maximum and minimum Reynolds number tests are shown in the left panels of Fig. 6. In both tests, which have similar maximum vorticity values, the maximum vorticity occurs at the leading edge. Note that the effects of the
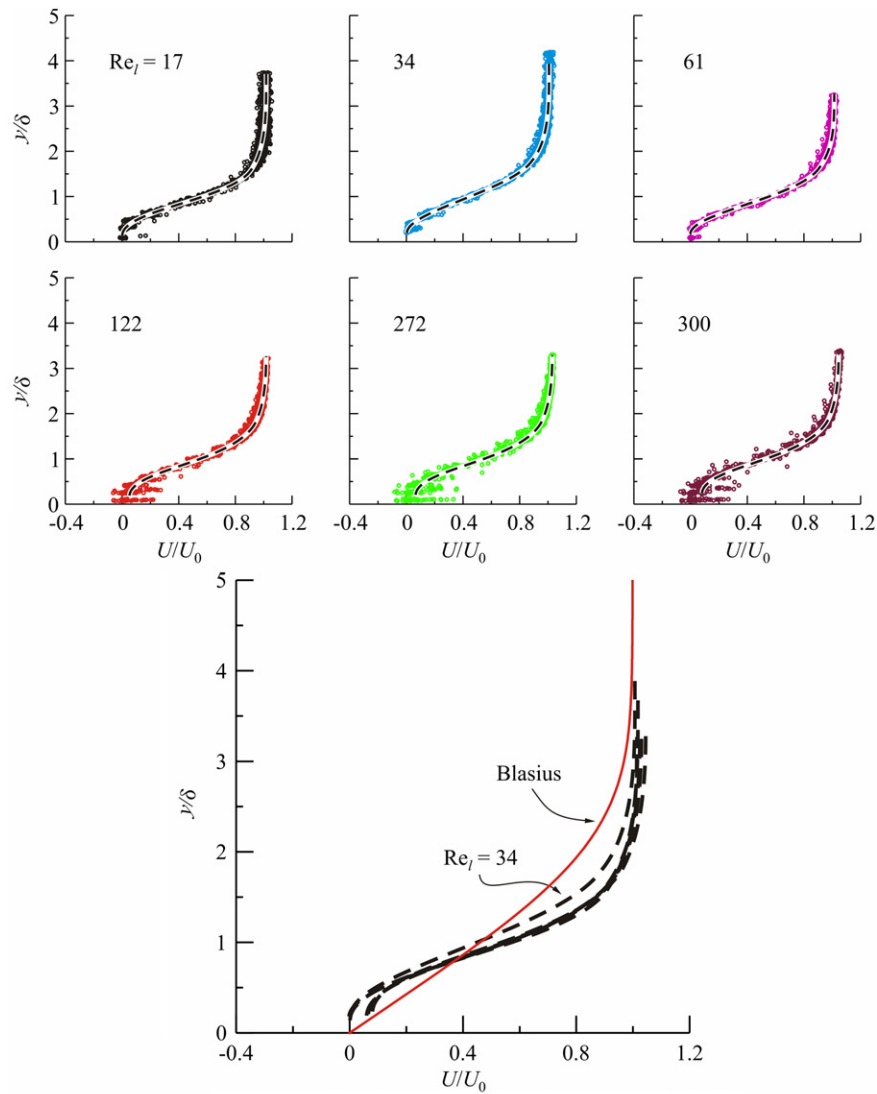
Fig. 5. Velocity profiles. The small panels contain the data measured for each test in 55 sections from the leading edge of the flat plate ($x = 0$) to almost the trailing edge ($x = -83$ mm). The large panel collects the interpolated profiles for all tests.

plate are also evident upstream, at a distance of more than 20 grain diameters for $Re_l = 17$ and at a minor distance for $Re_l = 300$. This effect, which has also been reported for bluff bodies in a granular mixture [11,12], is due partially to the finite thickness of the plate and partially to the development of frictional stresses that reduce the mobility of the sediments approaching the plate and modify the apparent shape of the plate. A small asymmetry is also evident between the boundary layers in the upper and lower sides of the plate.

The right panels of Fig. 6 show the vorticity computed with the Blasius equation, assuming an equivalent kinematic viscosity (Eq. (4)) for the mixture. While at higher Reynolds numbers there is a similarity between the patterns of vorticity in the granular mixture and in the Newtonian viscous flow, at lower Reynolds numbers, the patterns are significantly different. The absolute values of the vorticity are much smaller in the Newtonian viscous fluid and the vorticity is also much more diffused without the maxima observed near the leading edge for the granular mixture. Note that the details near the leading edge are missed because the Blasius solution is locally invalid where $Re_x = 0(1)$; it is also invalid near the trailing edge where it is influenced by the wake.

Fig. 7 shows the measured profiles of the vorticity (small panels) and the interpolated profiles of the vorticity for all of the tests at

several sections that range from the leading edge almost to the trailing edge. As for the mean velocity profiles, there is a significant similarity not only among the vorticity profiles at different sections but also among tests for different Reynolds numbers.

3.3. Divergence

The mixture has a bulk density that varies with the volumetric concentration of the grain; therefore, it can be considered compressible. A negative divergence is associated with an increasing volumetric concentration and vice versa. Fig. 8 shows the average non-dimensional divergence for the tests with minimum and maximum Reynolds numbers. Near the leading edge and near the surface of the plate, a negative divergence indicates that the grains are undergoing compaction, whereas a positive value indicates that the grains are dilating. Along paths that are parallel to the surfaces of the flat plate inside the boundary layer, positive and negative values of divergence suggest that a highly repetitive stick-and-slip behaviour of the grains dominates the sediment motion.

Indications of the spatial structure of the divergence are obtained by computing the power spectrum of the fluctuating divergence field in the wavelength domain. Fig. 9 shows the values for four tests along a path at $y = +10d$. Although the spatial resolution
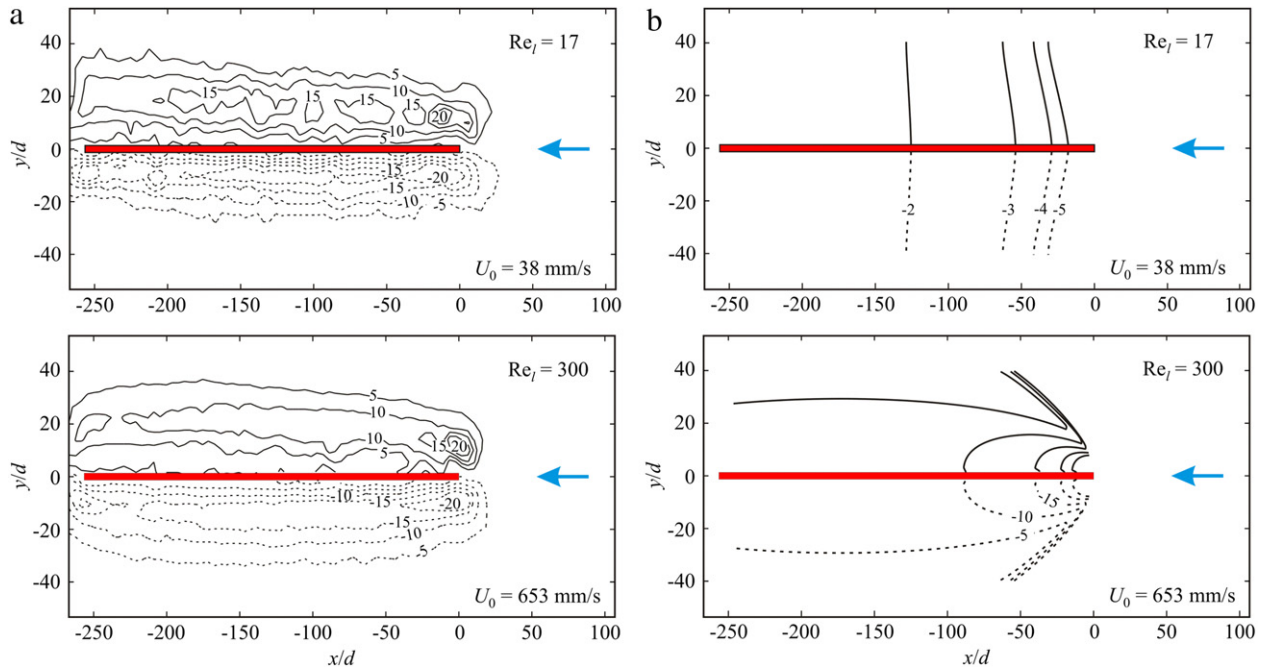
Fig. 6. Average non-dimensional vorticity $\omega_z l/U_0$. Left panels (a): present tests; right panels (b): Blasius solution for an infinite plate boundary layer. The dashed lines refer to clockwise vorticity.

is limited, two peaks are common to all tests, at wavelengths equal to $\lambda_1 \approx 32d$ and $\lambda_2 \approx 43d$. Since the tests at $Re_l = 17, 34$ show a spectrum without evident peaks (not shown), the phenomenon requires a minimum Reynolds number to trigger the periodic sequence of fluctuating divergence.

3.4. Spatial correlation

A measure of the spatial structure of the flow field is represented by the spatial correlation tensor. In certain experiments that measured the surface granular temperature in a shear granulator [16], a detailed discussion on the expected structure of the correlation function is reported. Essentially, according to [16] if the correlation refers only to self-correlation of the grains, a rapid decay of the function is expected at distances larger than the grain diameter, thereby making the application of the kinetic theory of granular flow reliable. It is expected that if the motion of the grains in the mixture develops with coherent structures larger than the grain itself, the correlation is still significant at distances larger than several grain diameters.

The double velocity spatial correlation is computed as follows:

$$\chi_{ij}(\mathbf{x}, \mathbf{x} + \mathbf{r}) = \overline{U_i'(\mathbf{x})U_j'(\mathbf{x} + \mathbf{r})}, \tag{9}$$

and in non-dimensional normalised form, this correlation becomes

$$R_{ij}(\mathbf{x}, \mathbf{x} + \mathbf{r}) = \frac{\overline{U_i'(\mathbf{x})U_j'(\mathbf{x} + \mathbf{r})}}{(\overline{U_i'^2(\mathbf{x})U_j'^2(\mathbf{x} + \mathbf{r})})^{1/2}}. \tag{10}$$

The over bar indicates the ensemble average. Having only two-dimensional measurements and neglecting $i \neq j$ implies that only two terms of the correlation tensor can be analysed:

$$R_{11}(x_0, y_0, x_1, y_1)$$
$$= \overline{U'(x_0, y_0)U'(x_1, y_1)}/(\overline{U'^2(x_0, y_0)U'^2(x_1, y_1)})^{1/2}$$

and

$$R_{22}(x_0, y_0, x_1, y_1)$$
$$= \overline{V'(x_0, y_0)V'(x_1, y_1)}/(\overline{V'^2(x_0, y_0)V'^2(x_1, y_1)})^{1/2},$$

in which (x_0, y_0) are the coordinates of a fixed point and (x_1, y_1) are the coordinates of the variable point. The available data allow the computation of the correlation along the generic directions with relatively good accuracy. In Fig. 10, the contour maps of the vertical velocity correlation are shown for points in the upper and lower boundary layers except for two points (point A and its correspondent symmetrical respect to the flat plate) that are positioned upstream of the leading edge. For the points inside the boundary layer (B, C, D and their correspondent symmetrical points), the extension of the contour lines is slightly larger in the direction normal to the wall with respect to the streamwise direction (parallel to the wall). Except for point B, which is influenced by the effects of the leading edge, the correlation has a non-zero value near the wall and has a weak symmetry with respect to the axis at $\pm 45°$, which is coincident with the principal axis of deformation. The two points upstream of the leading edge (point A and its symmetrical) show a high level of correlation at much larger distances than for points inside the boundary layer. These results are more evident in Fig. 11, which shows the correlations at the same points and for both the vertical and the horizontal velocity. The existence of spatial correlation and clustering on a scale that is much larger than the grain diameters is an indicator that granular gas-like dynamics at high volumetric concentrations have a limited adherence to reality. The experimental evidence of clustering was introduced in models of dry granular flows by [9], who suggested that in a slow, quasi-static regime, the correlation amongst grains is high; however, in a collisional regime, the correlation disappears and the random fluctuating motion of the grains increases the accuracy of a gas-like model. This correlation is due to the formation of granular eddies, which play the role represented in turbulence modelling by turbulent eddies; in stress–strain relations the mixing length is related to the integral length scale, which is computed as

$$L_{ij}(\mathbf{x}) = \int_{R=1}^{R=0} R_{ij}(\mathbf{x}, \mathbf{x} + \mathbf{r}) dr, \tag{11}$$

in which the limits of integration refer to the space lag values where the correlation is equal to unity and to zero. The integral
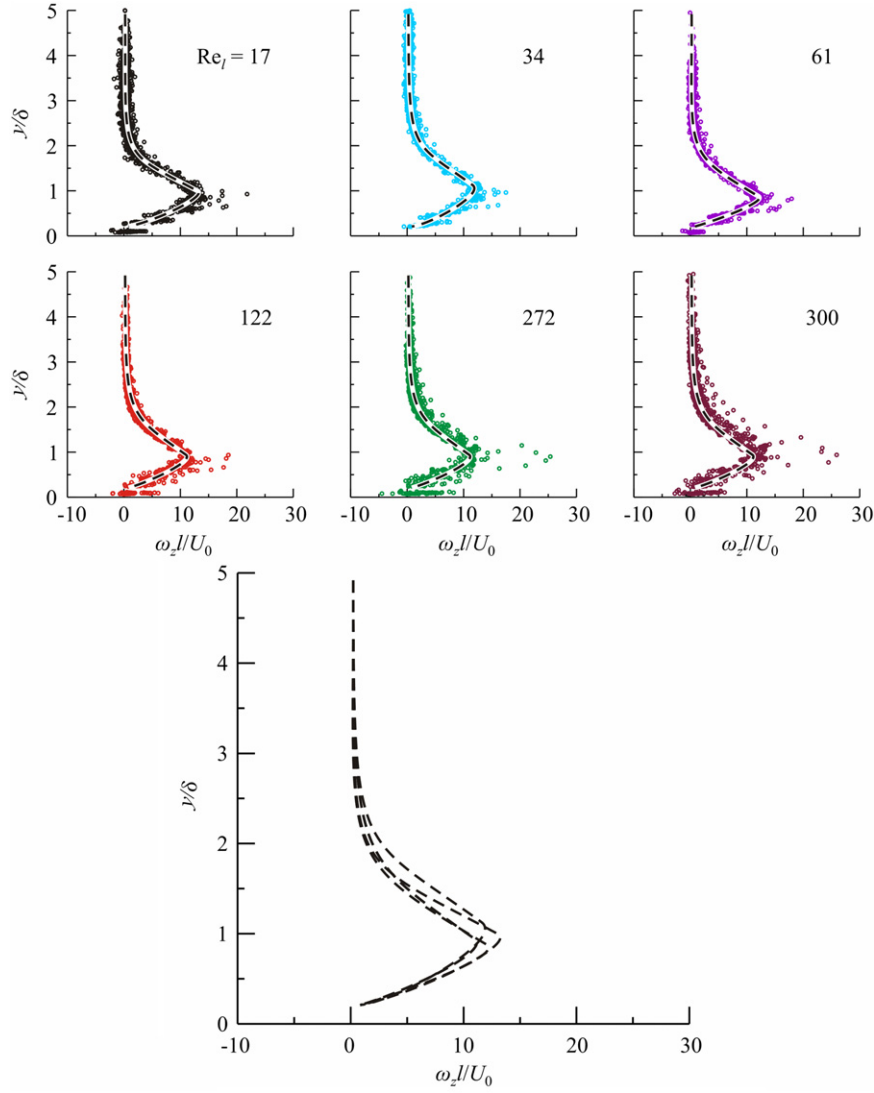
Fig. 7. Vorticity profiles. The small panels contain the data measured for each test in 55 sections from the leading edge of the flat plate ($x = 0$) to almost the trailing edge ($x = -83$ mm). The large panel collects the interpolated profiles for all tests.

length scale is a function of direction and of the fluctuating velocity components represented by subscripts i and j in the correlation, and in strongly anisotropic flows, it assumes different values in different directions. For modelling transport phenomena, the most suitable direction is represented by the direction where the most relevant flux takes place, i.e., the y direction in present experiments.

Fig. 12 show the integral length scales in the y direction that can be fitted with the functions

$$\frac{L_{y,UU}}{\delta} = a_1 \left(\frac{y}{\delta}\right)^{\alpha}, \qquad \frac{L_{y,VV}}{\delta} = a_2 \left(\frac{y}{\delta}\right)^{\alpha}, \tag{12}$$

in which $a_1 = 3, 4, a_2 = 1, 2$ and $\alpha = 0.82, 0.85$. The integral length scales in the streamwise direction (not shown) can be approximated with the same function as Eq. (12):

$$\frac{L_{x,UU}}{\delta} = a_3 \left(\frac{y}{\delta}\right)^{\alpha}, \qquad \frac{L_{x,VV}}{\delta} = a_4 \left(\frac{y}{\delta}\right)^{\alpha}, \tag{13}$$

and the growth is determined by the exponent $\alpha = 0.51, 0.55$, which yields $L_x \propto (L_y)^{\approx 0.6}$. If L_x and L_y are representative of the correlation lengths of the transient chains as described in [10], the

result should be $L_x \propto (L_y)^{1/2}$, with an exponent almost equal to the value 0.6 found in the present experiments.

4. Modelling the velocity profiles

The interpretation of the velocity profiles requires a proper model of the rheology of the mixture. Following [4], we assume that the stress tensor can be expressed as

$$\mathbf{T} = \mathbf{T}^0 + \mathbf{T}^*, \tag{14}$$

in which $\mathbf{T}^0$ is the equilibrium stress tensor, which is equal to the total stress tensor as the rate of deformation tensor $\mathbf{D} \to 0$, and $\mathbf{T}^*$ is defined as the dissipative part of the stress tensor. For the case of simple shear, the dissipative parts of the normal and tangential stress are equal to
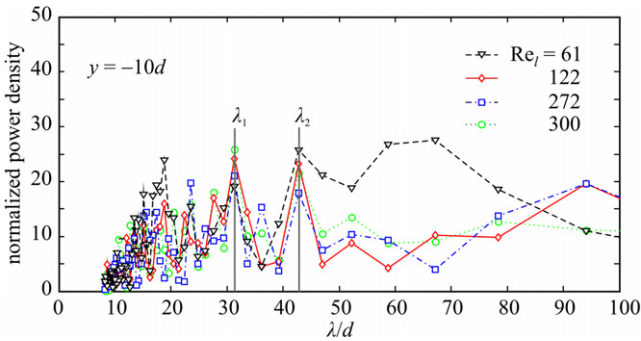
$$\sigma^* = \mu_0 \left(\frac{\partial U}{\partial y}\right)^2, \qquad \tau^* = \mu_1 \left|\frac{\partial U}{\partial y}\right| \left(\frac{\partial U}{\partial y}\right), \tag{15}$$

in which, on the basis of Bagnold's experiments, it is assumed that

$$\mu_0 = \beta_0 \left(\frac{C_* - C_0}{C_* - C}\right)^8, \qquad \mu_1 = \beta_1 \left(\frac{C_* - C_0}{C_* - C}\right)^8. \tag{16}$$
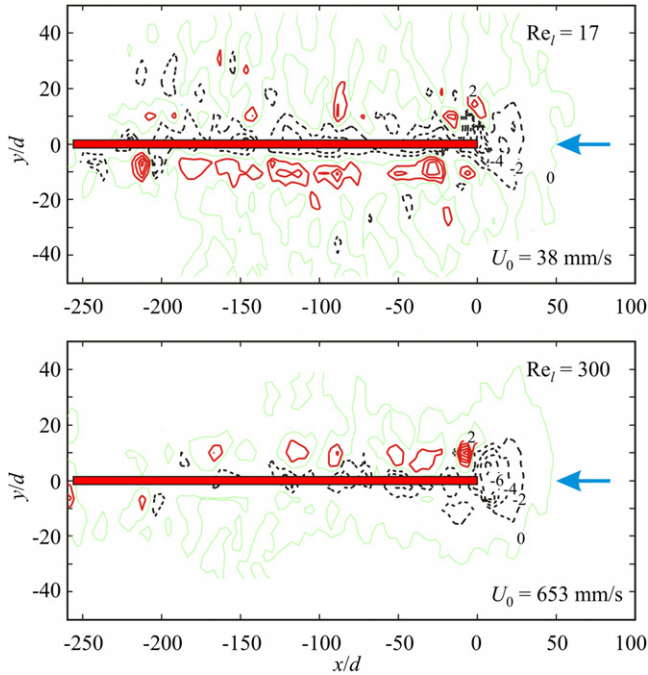
Fig. 8. Average non-dimensional divergence, $(\partial U/\partial x + \partial V/\partial y)l/U_0$. The dashed lines refer to negative divergence (sink), the thin lines refer to the zero divergence, and the thick lines refer to positive divergence (source).

Fig. 9. Non-dimensional power spectrum of the fluctuating divergence field evaluated at $y = +10d$ in the wavelength domain.

In Eq. (16), C_* is the densest possible volumetric concentration of the grains, C_0 is the volumetric concentration at which fluidity occurs, and β_0 and β_1 are constants. The structure of Eq. (16) is not critical; therefore, different functions can be adopted. The ratio

between the dissipative stresses is equal to

$$\frac{\tau^*}{\sigma^*} = \pm\frac{\mu_0}{\mu_1} \equiv \pm\frac{\beta_0}{\beta_1} \equiv \pm\tan\phi_D, \tag{17}$$

in which ϕ_D is the dynamic internal friction angle, which is assumed constant.

The equilibrium normal and tangential stresses are expressed as follows:

$$\sigma^0 = \chi\left(\frac{1}{b} + 1\right), \qquad \tau^0 = 0, \tag{18}$$

with

$$b = \begin{cases} k(C - C_0) & \text{for } C \geqslant C_0 \\ 0 & \text{for } C < C_0 \end{cases} \tag{19}$$

in which χ and k are constants.

By assuming homogeneity in the streamwise direction and neglecting the vertical velocity, the momentum balance equation in the vertical direction reduces to

$$\frac{\partial\sigma}{\partial y} = -\rho'_s g C, \tag{20}$$

in which ρ'_s is the submerged mass density of the sediment and g is the gravitational acceleration. The normal stress is assumed to be positive if compressive. Eq. (20) can be integrated by assuming a mean value of C, producing the vertical variation of the normal stress

$$\sigma = \sigma_h + \rho'_s g\overline{C}(h - y), \tag{21}$$

with h defined as the level where $\sigma = \sigma_h$. σ_h can be defined as a confining normal stress. By using Eqs. (15), (18) and (21), we may write
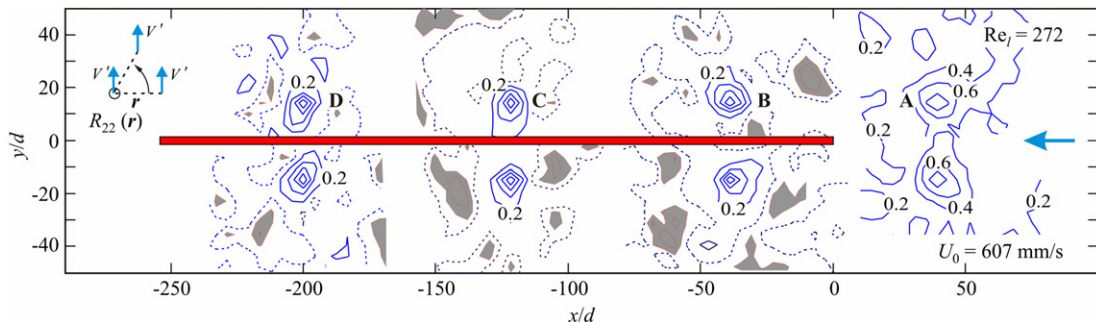
$$\chi\frac{1 + k(C - C_0)}{k(C - C_0)}\left(\frac{\partial C}{\partial y}\right)^2 + \mu_0\left(\frac{\partial U}{\partial y}\right)^2 = \sigma_h + \rho'_s g\overline{C}(h - y), \tag{22}$$

and introducing Eq. (17) yields

$$\chi\frac{1 + k(C - C_0)}{k(C - C_0)}\left(\frac{\partial C}{\partial y}\right)^2 = \sigma_h + \rho'_s g\overline{C}(h - y) - \frac{|\tau|}{\tan\phi_D}. \tag{23}$$

In Eq. (23) we assume that τ is the imposed uniform shear stress. Eq. (23) can be written as

$$\frac{1 + k(C - C_0)}{k(C - C_0)}\left(\frac{\partial C}{\partial y/h}\right)^2 = \frac{\sigma_h h^2}{\chi} + \frac{\rho'_s g\overline{C}h^3}{\chi}\left(1 - \frac{y}{h}\right) - \frac{|\tau| h^2}{\chi\tan\phi_D}. \tag{24}$$

Fig. 10. Contour maps of the spatial correlation of the vertical velocity for points A, B, C and D at $x = +40d, -40d, -120d, -200d$ and $y = +15d$ and their symmetrical at $y = -15d$. The thick lines refer to positive values, the dashed lines refer to zero value, the hatched areas refer to negative values, and contour steps equal to 0.2.
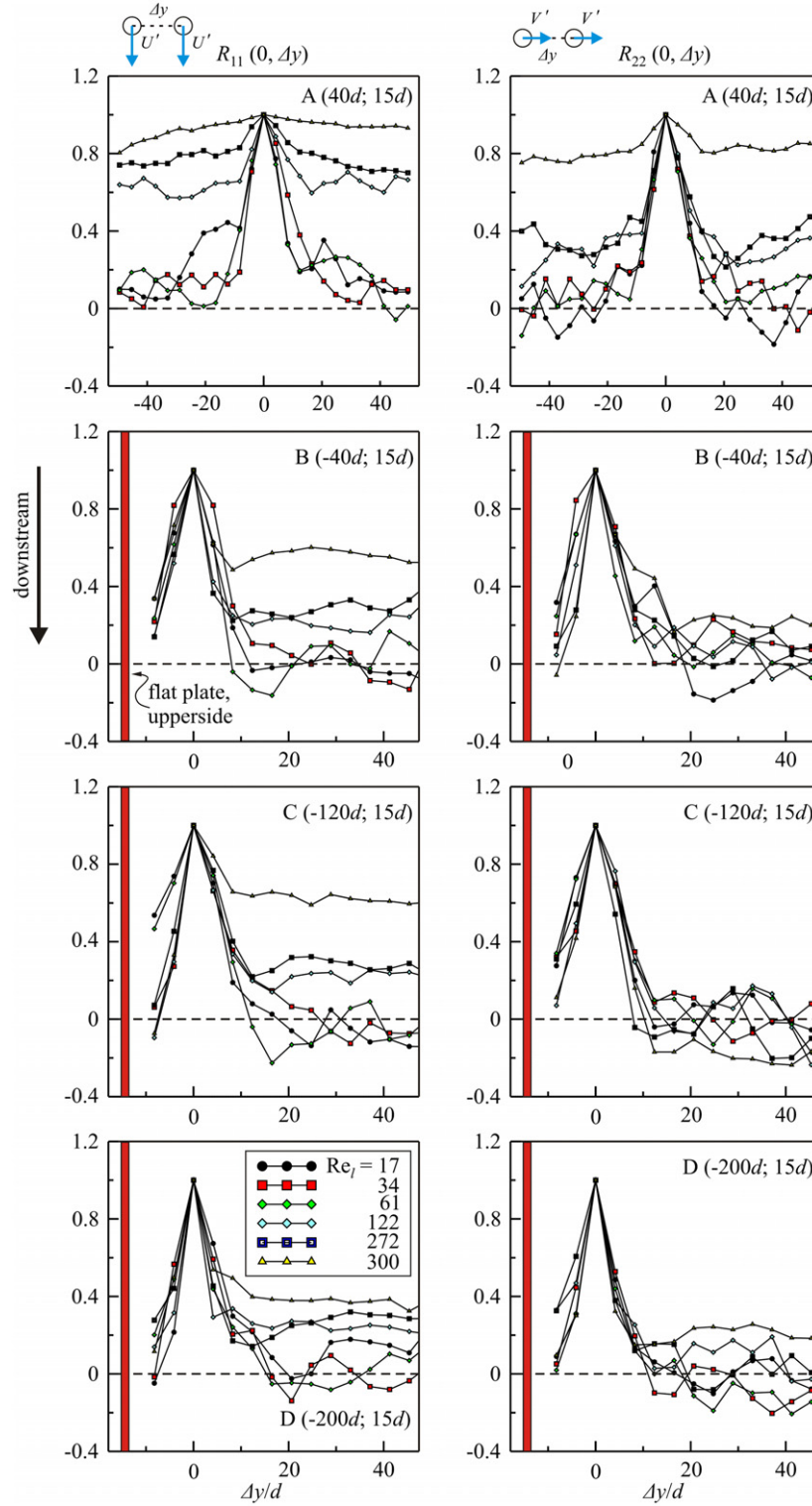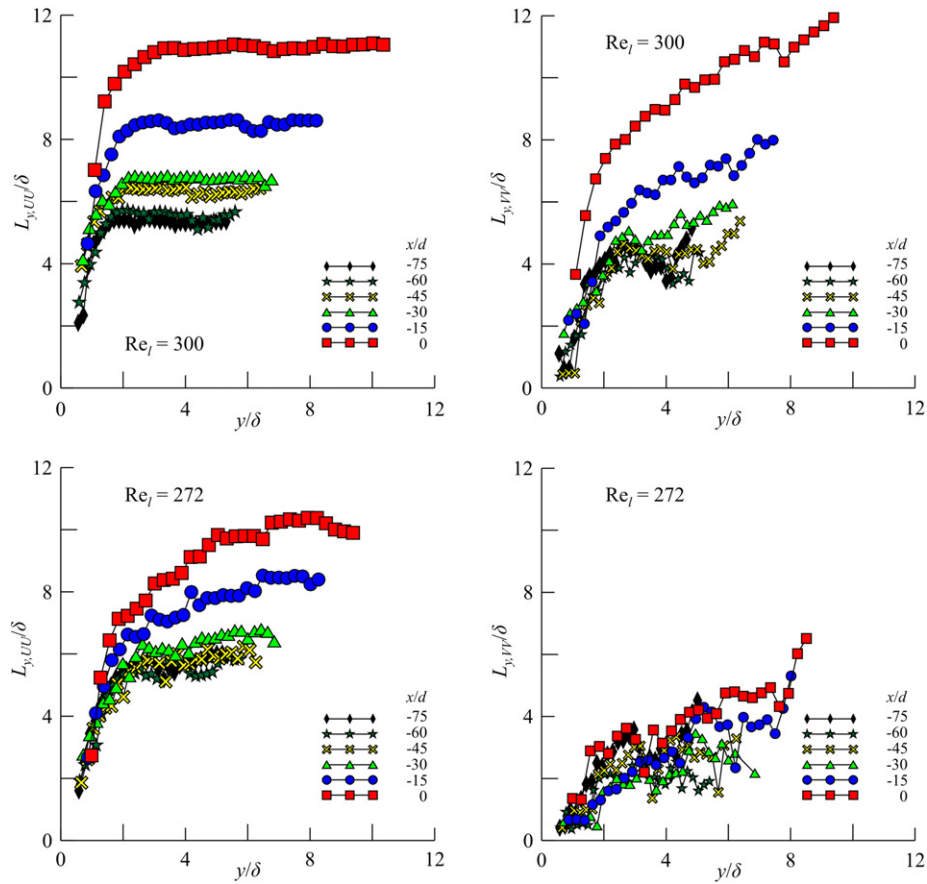
Fig. 11. Spatial correlation at points A, B, C and D at $y = 15d$ and different downstream locations (see Fig. 10). Point A is upstream the leading edge of the flat plate, points B, C and D are in the upper boundary layer. Left panels: correlation in the vertical for the streamwise fluctuating velocity. Right panels: correlation in the vertical for the spanwise fluctuating velocity.

χ is the limiting value of the equilibrium normal stress for $C \rightarrow C_0$ and is assumed to be the scale of the stresses, while h is the length scale. Hence, $\sigma_h h^2 / \chi$ indicates the relative importance of the confining normal stress, $\rho'_s g \overline{C} h^3 / \chi$ accounts for the relative importance of gravitational action and $|\tau| h^2 / \chi$ accounts for the relative importance of the imposed tangential stress.

The volumetric concentration of the sediment varies slightly through the depth and Eq. (24) may be approximated as

$$(C - C_0)^{-1/2} \frac{\partial C}{\partial y/h} = \pm \sqrt{\frac{\frac{\sigma_h h^2}{\chi} + \frac{\rho'_s g \overline{C} h^3}{\chi}\left(1 - \frac{y}{h}\right) - \frac{|\tau| h^2}{\chi \tan \phi_D}}{1/k + (\overline{C} - C_0)}}, \quad (25)$$

Fig. 12. Integral length normalised by the displacement thickness of the boundary layer in several sections for tests at $Re_l = 272, 300$. The left panels refer to the streamwise fluctuating velocity correlation, the right panels refer to the spanwise fluctuating velocity correlation.

in which the positive and the negative sign refer to the cases in which the volumetric concentration either increases or decreases in the vertical direction. By limiting the analysis to the second case, we also note that the argument within the square root is always positive if $C > C_0$. In compact form, Eq. (25) can be written as

$$(C - C_0)^{-1/2} \frac{\partial C}{\partial \tilde{y}} = \sqrt{\tilde{\sigma}_h + \tilde{g}(1 - \tilde{y}) - \tilde{\tau}}, \tag{26}$$

in which the denominator of the argument in the square root has been included in the non-dimensional groups. The symbol tilde indicates a non-dimensional variable. Eq. (26) may be integrated by imposing that the volumetric concentration equals C_0 at $y = h$, which yields

$$
\begin{aligned}
C = C_0 &+ \frac{2}{9\tilde{g}^2}(\tilde{\sigma}_h - \tilde{\tau})^3 - \frac{2}{9\tilde{g}^2}(\tilde{\sigma}_h - \tilde{\tau})^{5/2}\sqrt{\tilde{\sigma}_h + \tilde{g}(1 - \tilde{y}) - \tilde{\tau}} \\
&+ \frac{1}{3\tilde{g}}(1 - \tilde{y})(\tilde{\sigma}_h - \tilde{\tau})^2 \\
&- \frac{2}{9\tilde{g}}(1 - \tilde{y})(\tilde{\sigma}_h - \tilde{\tau})^{3/2}\sqrt{\tilde{\sigma}_h + \tilde{g}(1 - \tilde{y}) - \tilde{\tau}} \\
&+ \frac{1}{3}(1 - \tilde{y})^2(\tilde{\sigma}_h - \tilde{\tau}) + \frac{1}{9}\tilde{g}(1 - \tilde{y})^3.
\end{aligned}
\tag{27}
$$

Because the boundary condition $C = C_0$ at $y = h$ also requires $\tilde{\sigma}_h = \tilde{\tau}$, all terms in the right hand side are zero except the first and the last and Eq. (27) becomes

$$C = C_0 + \frac{1}{9}\tilde{g}(1 - \tilde{y})^3. \tag{28}$$

The condition $C_0 < C < C_m$ requires the flowing layer where the equilibrium stress is active to be limited by

$$1 - \left[\frac{9}{\tilde{g}}(C_m - C_0)\right]^{1/3} < \tilde{y} < 1. \tag{29}$$

Combining Eqs. (28), (15) and (16) yields

$$\left[1 - \frac{\tilde{g}}{9(C_* - C_0)}(1 - \tilde{y})^3\right]^{-8}\left(\frac{\partial \tilde{U}}{\partial \tilde{y}}\right)^2 = \frac{\tau h^2}{\beta_1 U_0^2}, \tag{30}$$

in which $\tilde{U} = U/U_0$ and U_0 is a reference velocity. Imposing a velocity equal to zero at $\tilde{y} = 1 - [9/\tilde{g}(C_m - C_0)]^{1/3}$ yields an analytical solution to Eq. (30) with a cumbersome expression. Fig. 13 shows the velocity profile normalised with respect to the velocity at the level h. The non-dimensional profiles are functions only of $\tilde{g}/(C_* - C_0)$, and the right-hand term in Eq. (30) influences only the dimensional velocity profiles. Slip occurs for $\tilde{g}/(C_* - C_0) < 9$.

The parameters in Eq. (30) can be refined to reproduce the experimental velocity profiles near the wall of plate, but a poor adherence is observed at large distances from the wall. In fact, the experimental non-dimensional velocity profiles in Fig. 5 show an inflection point with a change of curvature and a limited gradient at the edge of the boundary layer. The change in sign of the curvature represents an additional phenomenon that can be modelled by introducing the model proposed by Ertaş and Halsey [9], developed from a non-local rheology scheme of granular systems [10]. Ertaş and Halsey [9] proposed a modification of Bagnold's model by introducing a new length scale in place of the grain diameter,
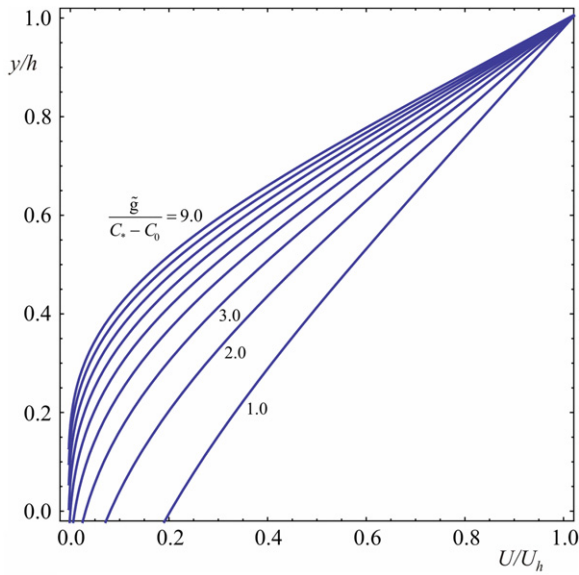
Fig. 13. Theoretical non-dimensional velocity profiles.

Table 2
Results of the best fitting procedure assuming $\alpha = 7/8$ and $(\tilde{\sigma}_h - \tilde{\tau})/(C_* - C_0)$, $\rho_s h^{2\alpha} a^2 / \beta_1$ as parameters.

Re_l	$\dfrac{\tilde{g}}{C_* - C_0}$	$\dfrac{\rho_s h^{2\alpha} a^2}{\beta_1}$
(.)	(.)	(.)
17	7.2	$10^{2.5}$
34	7.1	$10^{1.7}$
61	8.5	$10^{3.0}$
122	7.9	$10^{2.7}$
272	8.3	$10^{2.7}$
300	8.7	$10^{2.7}$

where the shear stress was proportional to a scale l_ν, defined as the viscosity length:

$$\tau = \rho_s l_\nu^2 (\partial_y U)^2. \tag{31}$$

Adopting the same scheme used in turbulence modelling, the viscosity length scale can be considered to be proportional to the

scale of the eddy and is often considered to be equal to the integral length scale. Because the experimental results demonstrate the integral length scale to be proportional to the distance from the wall of the plate (see Section 3), we can assume that $l_\nu = ay^\alpha$, in which $0 < \alpha < 1$ and a is a coefficient.

By additionally assuming that all the terms contributing to the shear stress are simply additive, in lieu of Eq. (30) we obtain the following differential equation:

$$\left[\left[1 - \frac{\tilde{g}}{9(C_* - C_0)} \left(1 - \tilde{y}\right)^3 \right]^{-8} + \frac{\rho_s h^{2\alpha} a^2}{\beta_1} \tilde{y}^{2\alpha} \right] \left(\frac{\partial \tilde{U}}{\partial \tilde{y}} \right)^2$$
$$= \frac{\tau h^2}{\beta_1 U_0^2}, \tag{32}$$

which can be numerically integrated by imposing a velocity equal to zero at $\tilde{y} = 1 - [9/\tilde{g}(C_m - C_0)]^{1/3}$. Based on the experimental results, we assume that $\alpha = 7/8$. Fig. 14 shows the non-dimensional velocity profiles computed for various values of the two non-dimensional groups controlling the process. In many profiles, the inflection point is reproduced.

A best-fit procedure has been applied to evaluate the two parameters under the assumption that $h = 2\delta$ and by using the experimental results. This last assumption is largely arbitrary, as concentration measurements would be required for a more consistent evaluation of h. The results of the procedure are listed in Table 2.

The computed values of the parameters reported in Table 2 have a limited range of variation, with the exception of the low Reynolds number tests. By assuming that the exponent α of the power law that expresses the vertical variation of the viscosity length scale is also a parameter, the optimisation procedure gives values of α that are much larger than unity (Table 3). If confirmed, this last result suggests that the viscosity length grows more than linearly with the integral length scale. The optimal velocity profiles for a single test at $Re_l = 122$ are shown in Fig. 15, with two curves computed by integrating the two- and three-parameter models with a best-fit procedure.

5. The vortices

In Newtonian fluid dynamics, eddies and coherent structures are responsible for a large part of the transport and on the same
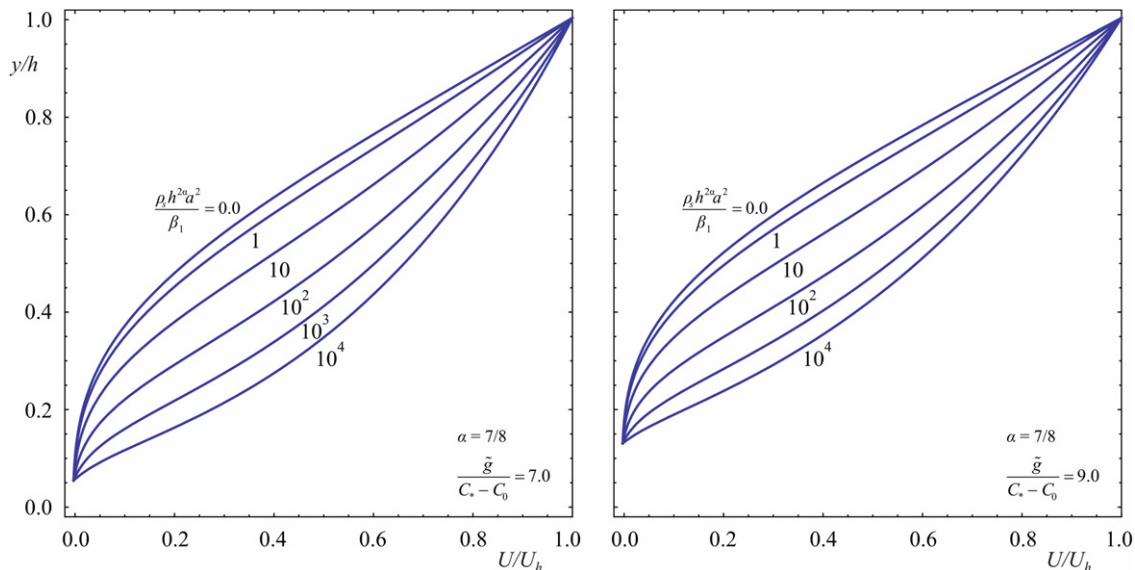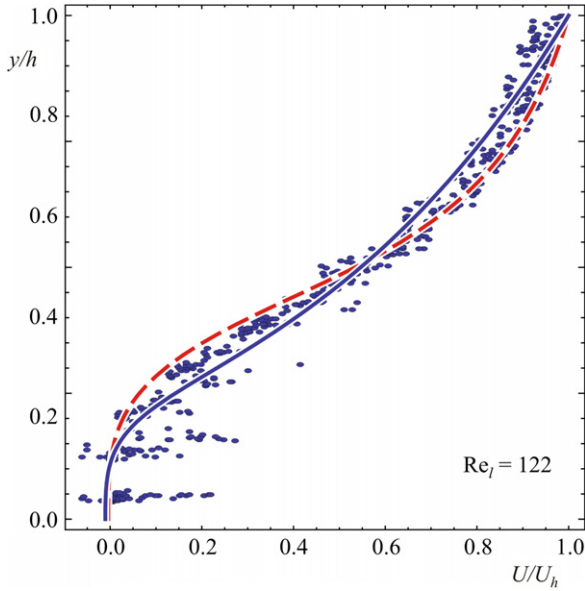

Fig. 14. Theoretical non-dimensional velocity profiles for two-dimensional horizontal flow, including the macro eddies contribution.

Fig. 15. Non-dimensional velocity profiles. Thick line: best fitting with the two parameters $(\tilde{\sigma}_h - \tilde{\tau})/(C_* - C_0)$ and $\rho_s h^{2\alpha} a^2/\beta_1$ with $\alpha = 7/8$; dashed line: best fitting with three parameters, including α. The values of the parameters are listed in Tables 2 and 3.

Table 3
Results of the best fitting procedure assuming $(\tilde{\sigma}_h - \tilde{\tau})/(C_* - C_0)$, $\rho_s h^{2\alpha} a^2/\beta_1$ and α as parameters.

| Re_l (.)	$\dfrac{\tilde{g}}{C_* - C_0}$ (.)	$\dfrac{\rho_s h^{2\alpha} a^2}{\beta_1}$ (.)	α (.)
17	7.0	$10^{2.4}$	2.5
34	7.0	$10^{1.6}$	1.3
61	7.0	$10^{2.4}$	2.4
122	7.8	$10^{2.5}$	2.0
272	8.0	$10^{2.5}$	2.3
300	8.0	$10^{2.5}$	2.6

line of the previous section, we assume that they are relevant also for granular mixtures. The detection of vortices is in itself a challenging task and there are numerous criteria based on phase-analysis, spatial correlation of vorticity, and other factors (see [11] for a list of references). The present approach is based on the λ_2-criterion given by Jeong and Hussain [17] and features an identification methodology based on the approach of Agrawal and Prasad [18]. The details and the algorithms are reported in [12]. Fig. 16 shows the spatial distribution of the computed vortices for the tests with the maximum and minimum Reynolds numbers. At low Reynolds numbers, the vortices are almost ubiquitous, but there is an evident separation in areas where clockwise (CW) or counter-clockwise (CCW) vortices dominate. At high Reynolds numbers, the vortices preferably develop at the edge of the boundary layer. Fig. 17 is similar to Fig. 16, but the radius is

proportional to the energy of the vortices. The spatial distribution indicates that at low Reynolds numbers, the vortices carrying significant energy are more frequent near the edge of the boundary layer with a progressive small increase moving downstream from the leading edge. At higher Reynolds numbers, clustering at the external edge of the boundary layer and near the leading edge of the flat plate is evident where the vortices have the maximum energy. The energy contribution of the vortices vs. the size is shown in Fig. 18 for the two extreme Reynolds number tests. The generation of vortices is more efficient for limited Reynolds numbers, and the average contribution of CW and CCW vortices is almost equivalent at low Re but is slightly different at high Re. This effect is due to the asymmetry of the upper and lower boundary layers, as a moderate gravitational action and the confining effect of the bottom wall of the experimental device slightly favours larger volumetric concentrations of the grains in the lower boundary layer. Furthermore, this effect apparently reduces the energy and density of the CW vortices. Separating the population for the upper and lower boundary layers (see Fig. 19) as expected indicates that in the upper boundary layer the most energetic vortices are CCW, while the opposite happens in the lower boundary layer. No preferential size of the vortices is selected, and the energy generally increases with the radius, with a possible limited reduction at larger values of the radius. In this respect, the present boundary layer differs from the boundary layers developed in presence of a triangular and circular cylinders [12], which were both characterised by a preferential radius of the vortices that generally varied with the Reynolds number.
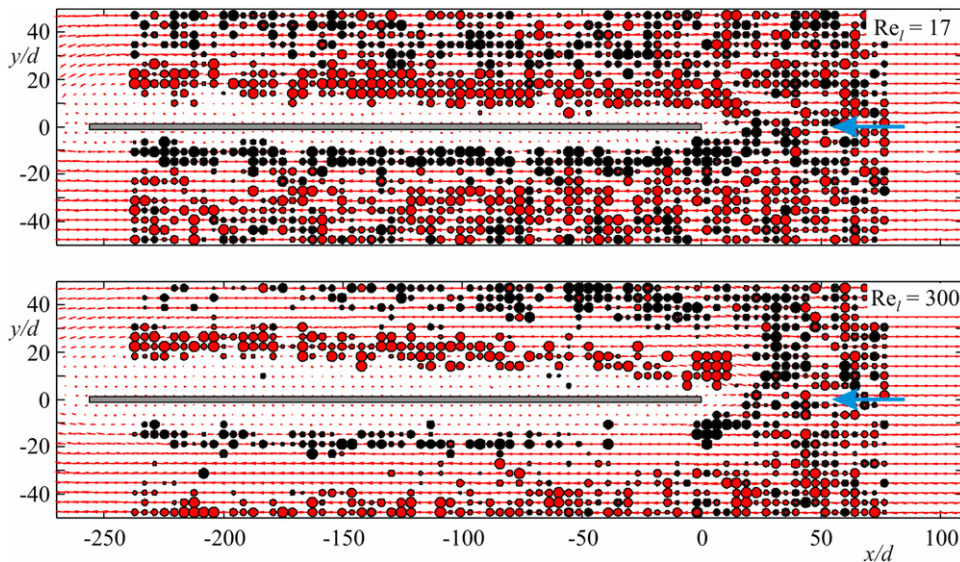
Fig. 16. Vortices detected for all frames. The size is proportional to the radius, arbitrary scale. Black: CW vortices; Grey (red): CCW vortices.
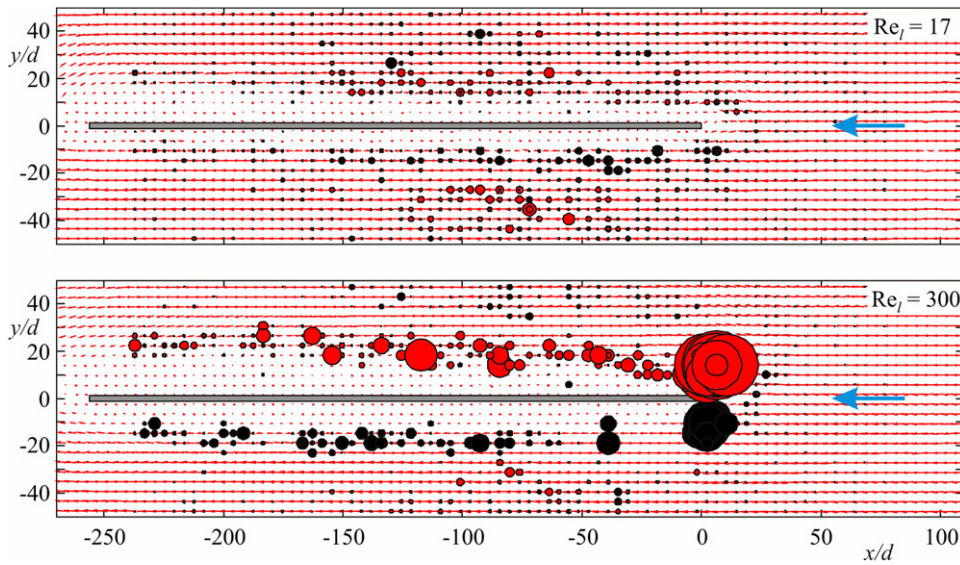
Fig. 17. Areal distribution of the vortices. The size is proportional to the absolute energy, arbitrary scale. Black: CW vortices; Grey (red): CCW vortices.
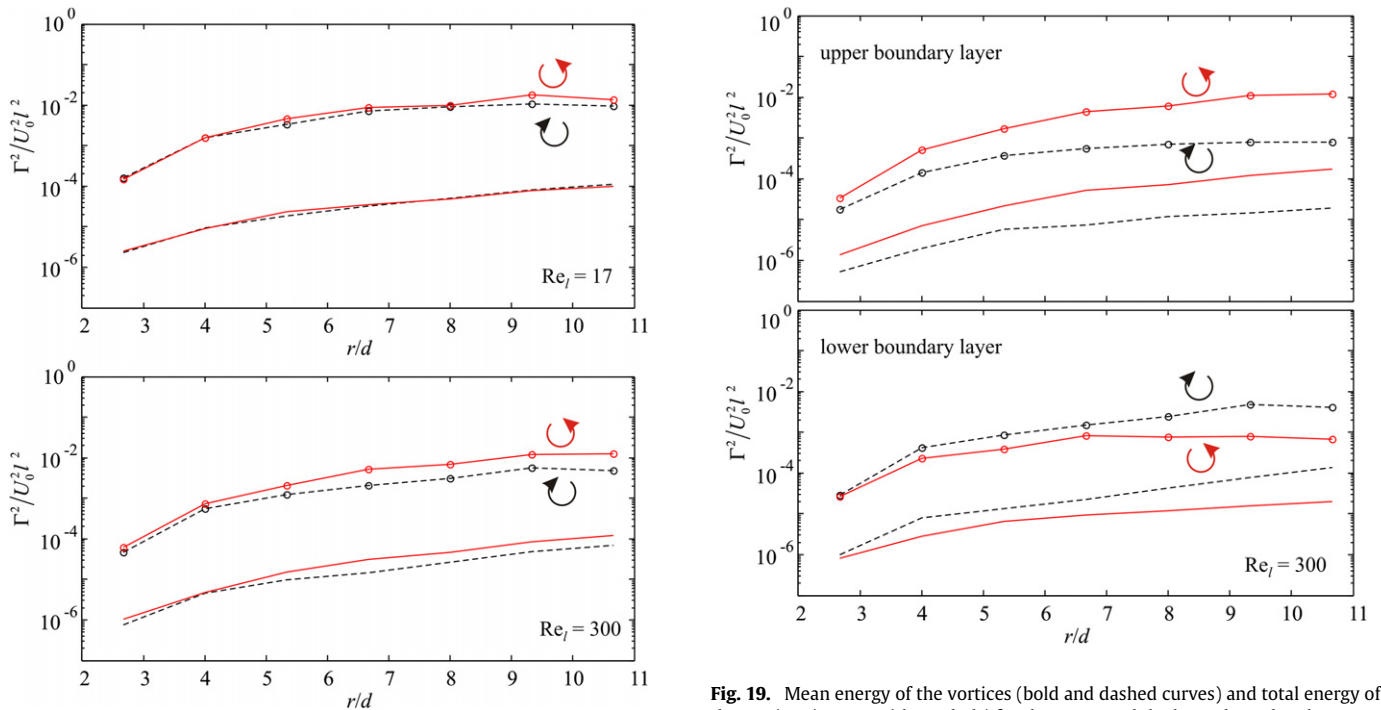

Fig. 18. Mean energy of the vortices (bold and dashed curves) and total energy of the vortices (curves with symbols) for the tests with the maximum and the minimum Reynolds number. Vortices detected including both the upper and the lower boundary layer.

Fig. 19. Mean energy of the vortices (bold and dashed curves) and total energy of the vortices (curves with symbols) for the upper and the lower boundary layer.

6. Conclusions

The overall pictures emerging from the present analysis indicates that the boundary layers in granular flows share many characteristics with the classical boundary layers in Newtonian fluids but with a behaviour largely controlled by the dominance of local scale or global scale phenomena. The experiments are novel and the results suggest that the analogies with turbulent phenomena and coherent structures, extensively studied in Newtonian fluid flows, are effective in explaining the observed behaviour of the complex grain–water mixture flows. A more extended and focused experimental activity is required to improve the knowledge of the subtle mechanisms behind grain–fluid–rigid walls interactions.

- We have measured velocity of a granular mixture with water as the inter-particle fluid in a 2-D stream past a thin, flat plate at zero incidence. Amongst the numerous parameters, the Reynolds number has been varied in a series of six tests with the same grain size, inter-particle fluid viscosity and static angle of repose.
- The flow field analysed with POD applied to both the velocity and the vorticity shows a high degree of organisation at high Reynolds numbers, with the emergence of dominant modes accounting for most of the energy of the flow field. At low Reynolds numbers ($Re_l < 61$), the energy is almost uniformly distributed amongst the modes.

- An upstream effect of the obstacle is observed, similar to that observed for bluff obstacles in similar conditions [11,12]. The displacement thickness and the momentum thickness of the boundary layer are slightly affected by the Reynolds number that was based on the length of the plate and show a slight increase downstream, beginning at the virtual origin located upstream with respect to the leading edge.
- The velocity profiles measured at different sections show remarkable self-similarity with respect to the displacement thickness of the boundary layer. The self-similarity is evident also amongst the mean profiles that correspond to different Reynolds numbers. Similar evidence also pertains to the vorticity profiles.
- The spatial correlations show an integral length scale in the vertical direction that is much larger than the grain diameters and proportional to y^α with $\alpha < 1$, y being the distance from the surface of the flat plate. The integral length scale in the direction parallel to the flat plate also growths with y, but to a lesser degree. These results are consistent with the formulation of granular eddies [9], which allow a non-local model of rheology (e.g., [10]).
- A model of the velocity profile based on Savage's model (1979), with the introduction of friction effects in a Bagnold's-like formulation of the tensor stress in the granular mixture and an additional turbulence-like model based on the Mills et al. and Ertaş and Halsey concepts of granular eddies, correctly reproduces the experimental velocity profiles.
- The vortices preferentially develop at the edge of the boundary layer at limited Reynolds numbers but also develop near the leading edge of the profile at larger Reynolds numbers. The vortices near the leading edge are the most energetic, and the detected vortices show no preferential size.

References

[1] A.A. Boateng, Boundary layer modeling of granular flow in the transverse plane of a partially filled rotating cylinder, Int. J. Multiph. Flow 24/3 (1998) 499–521.
[2] S. Longo, A. Lamberti, Granular shear flow mechanics, Exp. Fluids 32/3 (2002) 313–325.
[3] Z. Shojaaee, J.-N. Roux, F. Chevoir, D.E. Wolf1, Shear flow of dense granular materials near smooth walls. I. Shear localization and constitutive laws in the boundary region, Phys. Rev. E 86 (2012) 011301-1:12.
[4] S.B. Savage, Gravity flow of cohesionless granular materials in chute and channels, J. Fluid Mech. 92 (1979) 53–96.
[5] R. Artoni, A. Santomaso, P. Canu, Effective boundary conditions for dense granular flows, Phys. Rev. E 79 (031304) (2009) 1–6.
[6] R.A. Bagnold, Experiments on a gravity free dispersion of large solid spheres in a Newtonian fluid under shear, Proc. R. Soc. A 225 (1954) 49–63.
[7] S. Longo, Two-phase flow modeling of sediment motion in sheet-flows above plane beds, J. Hydraul. Eng. ASCE 131 (5) (2005) 366–379.
[8] D. Bonami, F. Daviaud, L. Laurent, M. Bonetti, J.P. Bouchaud, Multiscale clustering in granular surface flows, Phys. Rev. Lett. 89 (3) (2002) 034301-1-4.
[9] D. Ertaş, T.C. Halsey, Granular gravitational collapse and chute flow, Europhys. Lett. 60 (6) (2002) 931–937.
[10] P. Mills, D. Loggia, M. Tixier, Model for a stationary dense granular flow along an inclined wall, Europhys. Lett. 45 (6) (1999) 733–738.
[11] S. Longo, A. Valiani, L. Lanza, Experiments on the two-dimensional flow of a grain-water mixture past a circular cylinder, Eur. J. Mech. B Fluids 36 (2012) 139–151. Elsevier.
[12] S. Longo, A. Valiani, L. Lanza, D. Liang, Experimental study of the grain-water mixture flow past a cylinder of different shapes, Eur. J. Mech. B Fluids 38 (2013) 101–113. Elsevier.
[13] D. Liang, C. Jiang, Y. Li, Cellular neural network to detect spurious vectors in PIV data, Exp. Fluids 34 (1) (2003) 52–62.
[14] G.I. Taylor, Stability of viscous liquid contained between two rotating cylinders, Phil. Trans. R. Soc. A 223 (1923) 289–343.
[15] L. Sirovich, Turbulence and the dynamics of coherent structures. Parts I, II and III, Quart. Appl. Math. XLV(3) (1987) 561–590.
[16] G.K. Reynolds, A.M. Nilpawar, A.D. Salman, M.J. Hounslow, Direct measurement of surface granular temperature in a high shear granulator, Powder Technol. 182 (2008) 211–217.
[17] J. Jeong, F. Hussain, On the identification of a vortex, J. Fluid Mech. 285 (1995) 69–94.
[18] A. Agrawal, A.K. Prasad, Properties of vortices in the self-similar turbulent jet, Exp. Fluids 33 (2002) 565–577.